AIAA-2000-2524
Evaluation of New Camera Architectures for Pressure Sensitive Paint Measurements

Thomas F. Drouillard II, Chad W. Fisher,
Mark A. Linne, and Nigel T. Middleton
Center for Commercial Applications of Combustion in Space,
Colorado School of Mines, Golden, Colorado 80401-1887

Gregory J. Fiechtner and Larry P. Goss
Innovative Scientific Solutions, Inc.,
Dayton, Ohio 45433-7103

James R. Gord
Propulsion Directorate, U.S. Air Force Research Laboratory
Wright-Patterson Air Force Base, Ohio 45440-3638

21st AIAA Aerodynamic Measurement Technology and Ground Testing Conference
19-22 June 2000 / Denver, CO

EVALUATION OF NEW CAMERA ARCHITECTURES FOR PRESSURE SENSITIVE PAINT MEASUREMENTS

Thomas F. Drouillard II, Chad W. Fisher, Mark A. Linne, and Nigel T. Middleton
Center for Commercial Applications of Combustion in Space,
Colorado School of Mines, Golden, Colorado 80401-1887

Gregory J. Fiechtner and Larry P. Goss
Innovative Scientific Solutions, Inc., Dayton, Ohio 45433-7103

James R. Gord
Propulsion Directorate, U.S. Air Force Research Laboratory
Wright-Patterson Air Force Base, Ohio 45440-3638

Abstract

This work describes briefly the accepted techniques for obtaining and analyzing pressure sensitive paint (PSP) image data. It then presents interline transfer CCD (ITCCD) camera technology, and suggests improved PSP image data acquisition and analysis schemes based on this technology. Specifically, an ITCCD camera can make use of a double image feature that eliminates the need for a "wind-off" reference image. Double image data has been acquired. A more elaborate model of the fluorescence decay was developed, and a procedure for measuring pressure directly from image data is presented.

Initial laboratory studies have shown that an ITCCD camera can also be configured to acquire phase information when a periodic excitation source is applied to PSP. The details of such a system are presented.

Background

Pressure Sensitive Paint

PSP refers to a class of photo-reactive paints that fluoresce at a particular wavelength when exposed to light of a different (shorter) wavelength. As an example of a commercially available PSP, Innovative Scientific Solutions, Inc. (ISSI) manufactures products using a fluorinated platinum porphyrin species that absorbs visible short-wavelength (350 nm $\lesssim \lambda \lesssim$ 550 nm) incident light and fluoresces at longer visible wavelengths ($\lambda \approx$ 650 nm).[1] The fluorescence intensity and decay time depend on the temperature of the PSP and partial pressure of oxygen in contact with the PSP surface.

PSP Fluorescence Modeling

The Stern-Volmer fluorescence quenching model describes both the steady state and transient emission behavior of PSP.[2, 3] Equations (1) and (2) are respectively the time-integrated-intensity (steady state) and lifetime (transient) forms of Stern-Volmer equation as they are commonly represented in PSP literature.[3, 4, 5, 6]

$$\frac{I_A}{I} = 1 + K_{SV}\left[O_2\right] \tag{1}$$

$$\frac{\tau_A}{\tau} = 1 + K_{SV}\left[O_2\right] \tag{2}$$

where:

I_A = the time-integrated intensity of the fluorophore in the absence of a quenching agent (oxygen).

τ_A = the transient decay time constant of the fluorophore in the absence of a quenching agent (oxygen).

I = the time-integrated intensity of the fluorophore in the presence of a partial pressure of oxygen $[O_2]$.

τ = the transient decay time constant of the fluorophore in the presence of a partial pressure of oxygen $[O_2]$.

K_{SV} = the Stern-Volmer coefficient: a physical parameter specific to a fluorescent species with units inverse to that of the partial pressure of oxygen.

The most common use of PSP is in pressure experiments where the concentration of oxygen does not change but the total atmospheric pressure varies. In this case, the atmospheric pressure $p \propto [O_2]$ and the right-hand sides of equations (1) and (2) are both expressed as $1 + kp$.

The Pressure Sensitive Paint Technique

PSP experiments are commonly performed in an environment where an oxygen-free reference measurement is impractical (*e.g.*, a wind tunnel). The pressure sensitive paint technique has been developed as an alternative to removing the oxygen from a wind tunnel or other experiment environment.[5, 7, 8, 9] Wind tunnel PSP imaging experiments usually include a "wind-off" image that is used as a reference. In the absence of air flow, air pressure (and thus the partial pressure of oxygen) is constant. In a temperature-controlled experiment (one where the temperature is maintained constant between wind-off and wind-on imaging), pressure p is measured relative to the wind-off pressure p_{ref} by the ratio of the fluorescence intensity I relative to the wind-off intensity I_{ref}, as shown in equation (3),

$$\frac{I}{I_{ref}} = \frac{1 + k\,p_{ref}}{1 + k\,p} \qquad \textbf{(3)}$$

Accuracy and Error Assessments

Detailed uncertainty analyses of PSP measurements have been published by Sajben and by Donovan *et al.*, both in 1993.[5, 8] These articles typically focus on the accuracy of the ratio described in equation (3) from an observational perspective, emphasizing that this is the greatest source of error in the traditional PSP technique. Oglesby *et al.* also address the issue of uncertainty in PSP measurements, ascribing the Stern-Volmer model as the chief source of error.[4]

The fundamental source of error in the Stern-Volmer analysis of PSP data is based in the physics of the fluorescence behavior. A simplified fluorescence model states that incident light of a particular wavelength excites electrons of a fluorescent molecular species to a higher energy state. They decay to an intermittent state by vibrational relaxation (transferring energy to a vibrational mode) or by tunneling. Then relaxation back to a ground state occurs with photon emission. In this simple model, fluorescence decays exponentially from an initial fluorescence intensity I_A to zero at a rate (in the absence of any quenching agents)

controlled by the decay lifetime τ_A. In practice however, there are many other factors, most of which are environmental, that effect fluorescence decay. Quenching (interaction of the excited-state fluorophore with other species) reduces fluorescent emissions. PSP analysis relies on the effect of oxygen quenching on fluorescence to detect the partial pressure of oxygen. However, an excited-state species can undergo energy transfer by mechanisms other than fluorescence and quenching. Furthermore, fluorescence is affected by chemical inconsistencies or impurities and matrix effects of the solid-phase fluorophore. The resulting fluorescence decay is more accurately modeled by a sum of exponentials rather than by a single exponential.[3]

Another source of error in PSP experiments lies with the imaging system. A CCD array is subject to thermal noise, where charge accumulates due to thermal energy rather than by photons incident on the sensor. Furthermore, since the accumulated charge is digitized and read as a discrete number of *counts*, there is error associated with the analog-to-digital conversion. Minimization of error attributed to these factors is detailed in the discussion that follows.

Instrumentation

The items described in the following discussion refer to a CCD camera system, model 1300YHS-DIF, manufactured by Roper Scientific/Princeton Instruments, Inc. The hardware components that comprise the imaging system include a proprietary serial interface card installed in a PC, a camera controller unit connected to the serial card, and a camera head. In addition to the hardware items, user access to the imaging system features and operations is gained through the WinView/32 software package also provided by Roper Scientific/Princeton Instruments, Inc.

Camera Controller

The controller receives timing signals either from the computer or from external trigger sources and accordingly sends control signals to the camera to begin and end image acquisition. After images are acquired in the CCD array, the analog image data is downloaded to the controller where it is digitized and directed to the PC for storage as a data file. Digitization is accomplished by a 12-bit analog-to-digital converter such that the light intensity recorded by a CCD pixel is rendered as an integer ranging from 0 to 4095. The units of digitized intensity are referred to as counts. The

American Institute of Aeronautics and Astronautics

accuracy of the analog-to-digital converter as reported by Roper Scientific is 1-1.6 counts RMS and the linearity deviates by less than two percent.[10]

Two connectors on the controller that are used in the experiments that follow are the $\overline{\text{READY}}$ output and the EXT SYNC input. When the image acquisition routine is started, the $\overline{\text{READY}}$ output stays at a high TTL level until the camera is ready to acquire data, then it goes low, at which time, a TTL pulse applied to the EXT SYNC input initiates image acquisition.

Double Image Timing Modes

A camera equipped with the double image feature (DIF) offers three timing modes for gathering sequential exposures. The operational modes are described in Table 1. The timing mode most appropriate to a particular experiment is selected and configured in the WinView/32 software.

Table 1 Dual image camera exposure timing modes

Timing Mode	Description
IEC Internal Exposure Control	• Exposure time for both images equal, set in software. • Second exposure also includes 8 ms for shutter to close. • Second exposure begins immediately after first ends.
EEC External Exposure Control	• First exposure time determined by duration of external pulse. • Second exposure time set in software, plus 8 ms for shutter to close. • Second exposure begins immediately after first ends.
ESABI Electronic Shutter Active Between Images	• Both exposure times are equal and set in software. • Second exposure also includes 8 ms for shutter to close. • Exposures triggered by separate external pulses. • Separation time between exposures can be set via separation of external pulses.

Camera Head and CCD Architecture

The camera head encloses the CCD array, the shutter mechanism, and the mechanical and thermoelectric cooling components. The CCD array is thermally coupled to a Peltier cooling device that maintains the temperature of the array. Heat removed from the CCD array is dissipated by cooling fins on the camera housing and by a low-vibration electric fan. The cooling system is designed to maintain the temperature of the CCD at –15°C, thereby greatly reducing the effects of thermal noise in the array. Thermal noise decreases exponentially with temperature, and this noise level is reduced by approximately half per 6° reduction in temperature in the region at which a CCD camera is operated (+25° to –15°).[10]

A DIF camera captures two consecutive and separate images on the CCD chip prior to readout. The CCD array used in the imaging system is an interline transfer CCD, manufactured by Sony. The CCD, model *ICX061*, is a ⅔-inch progressive-scan image sensor. This CCD has 1300 horizontal pixels and 1030 vertical pixels, and each pixel is 6.7 μm square.[10]

The ITCCD demonstrated in Figure 1 has interlaced active columns and masked columns and is fitted with a micro-lens array. Photoelectrons collected in the active columns are transferred to adjacent masked columns for readout. Once the photoelectrons are in the masked column, referred to as the vertical register, they can then be read from the array without serious smearing effects and without adding further photoelectrons that would be considered noise.[11,12]
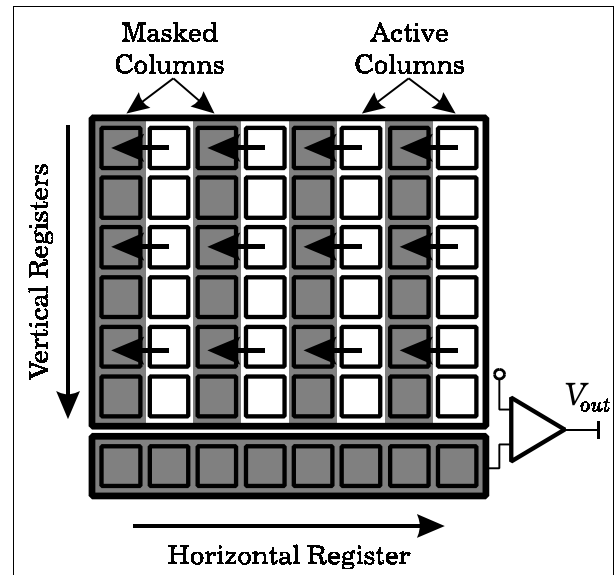

Fig. 1   Interline transfer CCD architecture

Also included in the ITCCD's structure is a variable speed, electronic shutter. The electronic shutter provides a means to clear any accumu-

lated photoelectrons and essentially reset the photo-sensor prior to an exposure interval. And, since the ITCCD has masked columns adjacent to the active sensors, the exposure time can be accurately controlled, resulting in a device does not require a mechanical shutter.[12]

In order to better facilitate discussion about charge flow, the two dimensions x and z are considered along the same axis, as illustrated in Figure 2 (physically, the substrate is beneath the sensor and register, hence the physical x direction would be downward). This figure shows the potential wells for the sensor, substrate, and vertical register. Between the wells are electronic barriers that prevent charge from moving. The overflow drain (OFD) barrier prevents the charge from moving from the sensor to the substrate, and the readout gate (ROG) barrier prevents the charge from moving from the sensor to the vertical register. The OFD and ROG barriers are controlled by the substrate voltage V_{sub} and the vertical register gate voltage V_{g2}, respectively.[13]
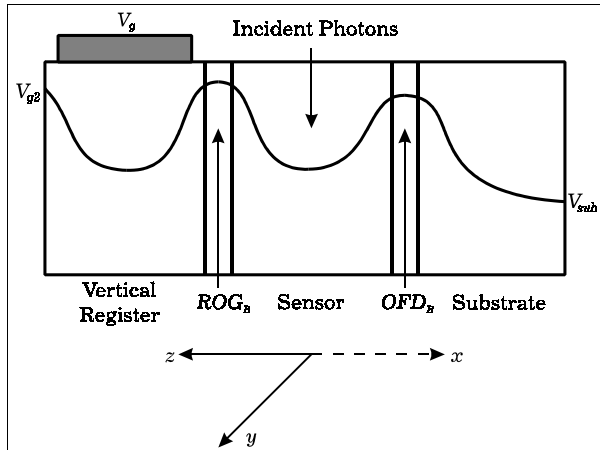

Fig. 2   **Simplified cross-sectional schematic of a single interline transfer CCD pixel. Note by the axes that the substrate is physically below the vertical register and sensor.**

Charge Flow Under Normal Operation

Figure 2 shows the configuration of an ITCCD pixel from a systematic perspective. The following treatment of charge flow is based on Figure 2. A detailed discussion of semiconductor-controlled charge manipulation in a pixel as implemented in this hardware is available from Sony.[14]

In a normal image acquisition process, the OFD barrier is initially lowered. This forces all charge accumulated in the sensor to immediately drain into the substrate. Thus, the electronic

shutter mechanism is controlled with the OFD barrier.

An image is then captured by raising the OFD barrier. Once this barrier is raised, all photoelectrons are accumulated in the sensor area. After the specified exposure time has elapsed, which began when the OFD barrier was raised, the charge packet accumulated in the sensor is shifted to the vertical register by lowering the ROG barrier.

The vertical register is covered by an aluminum mask that prevents photons from entering directly into the vertical register. Charge must first accumulate in the photo sensor area and then transferred to the vertical register. The same is true for the substrate, charge can be transferred to the substrate from the sensor, but cannot be created directly in the substrate.

After the charge packet is stored in the vertical register, the ROG barrier is then raised, thereby isolating the charge in the vertical register. The OFD barrier is once again lowered to drain new photoelectrons generated in the sensor. Finally, the charge packet stored in the vertical register is transferred, along the y direction, out of the CCD and digitized in the controller. While the image is being read out of the array, the process starts again and the next exposure is integrated in the sensor.

Charge Flow Under Dual Image Operation

Based on the ITCCD architecture and the previous discussion, the ITCCD can be used to capture two separate images with a short temporal difference. As shown in Figure 2, incoming photons are continuously converted to photoelectrons in the photo sensor area. The photoelectrons in the sensor area can be transferred either to the vertical register or to the CCD's substrate by actively controlling the ROG barrier and the OFD barrier.

In order to capture two separate images, the OFD barrier is initially lowered to drain photoelectrons into the substrate as they are generated. When a trigger initiating the capture of the first image is received at the controller, the OFD barrier is raised and the ROG barrier is simultaneously lowered. Photoelectrons generated in the sensor now migrate directly into the vertical register. The ROG barrier remains in the low position for the exposure time specified for the first image.

After the first image exposure time has elapsed, the ROG barrier is raised. Depending on the

American Institute of Aeronautics and Astronautics

configured timing mode (IEC, EEC, or ESABI) the OFD barrier is either held at its high position or once again lowered. If the OFD barrier is held at its high position after the ROG barrier is raised, the second image is stored in the sensor area immediately after the first exposure has concluded. In this case (IEC or EEC mode) the temporal separation between the two images is the time it takes to raise the ROG barrier, which is approximately 200 ns.[10]

When using the ESABI timing mode, the OFD barrier is lowered as the ROG barrier is raised, which concludes first image exposure time. A second trigger, initiating the capture of the second image, instructs the system to raise the OFD barrier. Once the OFD barrier is raised, the second image will be captured in the sensor area. Thus, if there is an ESABI delay between the two images (much larger than 200 ns) then photoelectrons accumulated during the interim between the conclusion of the first exposure and the beginning of the second exposure period are drained to the substrate.

After the images are captured, the first image is read from the chip and digitized in the same manor as with a single exposure readout. Once the first image has been read from the array, the ROG barrier is quickly pulsed low, transferring the second image, held in the sensor area, to the vertical register. The second image is then read from the chip and digitized.

The second image is captured and held in the sensor area, which is continuously exposed. While the first image is read from the array, any additional photoelectrons, generated from additional incident radiation accumulate in the second image. A mechanical shutter can be used to limit the exposure time to approximately 8ms.

Double Image PSP Experiments

Two experiments were conducted at ISSI in Dayton, OH. Both used the same laboratory setup described as follows. A surface painted with PSP was placed in a vessel where static atmospheric pressure was varied. The sample was illuminated with the frequency-doubled output from a Nd:YAG laser. Sequential images were acquired with the double-image feature using the IEC and ESABI modes, where pressure and exposure separation time were each varied.

Apparatus

The DIF camera head was fitted with a C-mount/F-mount adaptor, to which a Nikon AF Micro-Nikkor 105 mm lens was attached. A square of sheet aluminum painted with PSP was held in a vacuum vessel. The PSP used was the Pt(TfPP) from ISSI introduced earlier in this work. The pressure inside the vessel was maintained by a computer-controlled PID feedback system that controls a roughing pump easily capable of varying the pressure between 10 and 100 kPa. The vacuum vessel was fitted with viewports on two orthogonal sides for transverse optical access. The camera was arranged to view the PSP sample through one viewport while an excitation source was directed through the other. Fluorescence was induced by 532 nm light from a frequency-doubled 10 Hertz Q-switched Nd:YAG laser. Uniform illumination of the sample was achieved by passing the laser through a 10 degree light-shaping diffusion element, and an RG-645 colored glass filter in front of the camera lens stopped the excitation light from entering the camera. These components are illustrated in Figure 3.
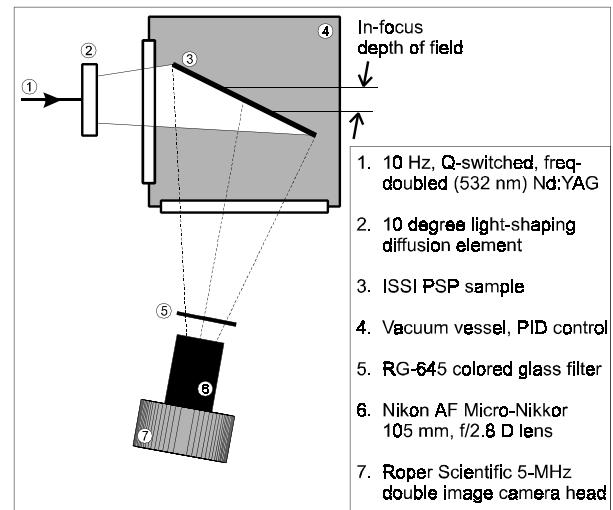

1. 10 Hz, Q-switched, freq-doubled (532 nm) Nd:YAG

2. 10 degree light-shaping diffusion element

3. ISSI PSP sample

4. Vacuum vessel, PID control

5. RG-645 colored glass filter

6. Nikon AF Micro-Nikkor 105 mm, f/2.8 D lens

7. Roper Scientific 5-MHz double image camera head

Fig. 3   Double image camera apparatus configuration for delay ramp and pressure ramp data.

Timing Configuration

The timing scheme used in these experiments is illustrated in Figure 4. The components in this figure include four DG-535 four-channel digital delay/pulse generators manufactured by Stanford Research Systems, an ORTEC 418A universal coincidence box made by EG&G (this implements the AND gate), and the camera controller from Roper Scientific/Princeton Instruments, Inc. Each DG-535 has two programmable outputs. One is the *A-B* output and the other is the *C-D* output. The programming for each channel used

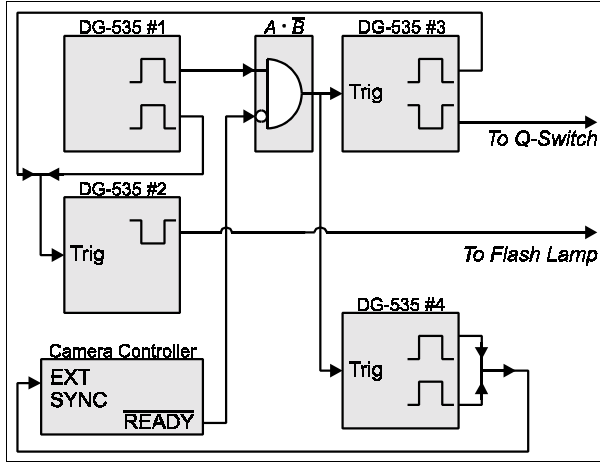in this experiment and the trigger settings for all four delay/pulse generators appear in Table 2.

Fig. 4   Timing schematic for dual image experiments.

Table 2   DG-535 Channel Settings

	DG-535 #1	DG-535 #2	DG-535 #3	DG-535 #4
Job	10 Hz	Flash Lamp	Q-Switch	Frame Ctrl
Trig	int	ext	ext	ext
A-B	⊓	⊔	⊓	⊓
A	T + 0.0	T + 0.0	T + 99.9 ms	T + 100.006 ms
B	A + 10 μs	A + 20 μs	A + 10 μs	A + 5 μs
C-D	⊓		⊔	⊓
C	T + 0.0	Not used	A + 165 μs	A + 90 μs
D	C + 10 μs		C + 10 μs	C + 5 μs

The general idea behind this timing configuration will be stated, where the details can be obtained by concurrently studying Figure 4 and Table 2. The Q-switch of the Nd:YAG laser requires a 10 Hertz pulse train to maintain consistent output intensity from one pulse to the next. This is provided by DG-535 #1. The 10 Hertz signal triggers DG-535 #2 which fires the flash lamp, and also triggers DG-535 #3 which fires the Q-switch.

Since there is some width to the 10 Hertz signal in the frequency domain, the precise temporal location of any one edge in the 10 Hertz pulse train is not known with sufficient precision that exposure sequences could be accurately timed from it. Both images however are acquired in less than 8.5 ms during the longest ESABI

sequence used in this experiment, where the 10 Hertz pulse train generates pulses separated by approximately 100 ms. Therefore, the camera controller is configured to produce a trigger at some point between two of the 10 Hz pulses. The temporal location of this forced trigger is known with precision less than ten ns. It fires the Q-switch and flash lamp, thereby producing a laser pulse between two of the 10 Hertz pulses. The forced trigger also signals DG-535 #4 to produce IEC or ESABI triggers that initiate image acquisition.

The IEC and ESABI exposure modes were used for double-image accumulations. The IEC mode was used to acquire images with no separation while the ESABI mode allowed a separation Δt, specified as appropriate for each experiment. Figure 5 illustrates the ESABI timing mode; the IEC mode is functionally the same as the ESABI mode with Δt set to zero. In the software, t_{exp} is specified and applies to both images, with the understanding that 8 ms is added to the second exposure duration. Thus if $t_{exp} = 10\,\mu$s (as in the following experiments), the second exposure is 8.01 ms.
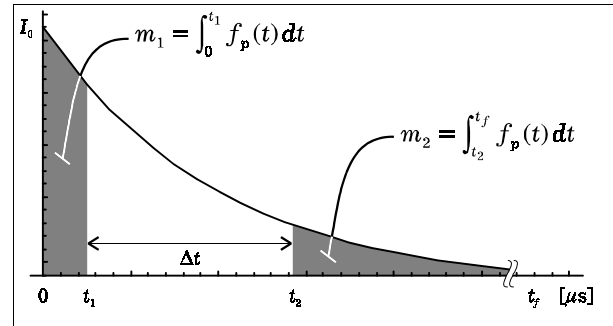

Fig. 5   ESABI double image acquisition of exponential fluorescence decay. Each exposure represents the integrated fluorescence over the duration of the exposure. Under the ESABI setting, the first exposure is 10 μs and the second is 8.01 ms. The ESABI mode with a separation $\Delta t =$ 0 is behaviorally the same as the IEC mode.

PSP Image Data Acquisition

The apparatus described by Figure 4 and Table 2 was used to acquire image data for both experiments. Figure 6 shows a pair of PSP images. Note that the printed quality of Figure 6 is of significantly lower spatial and grayscale resolution than the image data stored in a WinView/32 file (1300 pixels × 1030 pixels × 4095 counts).

For both experiments, the ESABI (or IEC as appropriate) exposure duration was set to 10 μs in the WinView/32 software. Therefore, the first

exposure is 10 μs and the second exposure is 8.01 ms (10 μs + 8 ms for the shutter to close) for all image pairs.

Another system parameter of importance and common to both experiments is the ADC OFFSET value specified in the WinView/32 software. This parameter offsets the readout voltage (proportional to the CCD charge values) by a fixed, constant amount. The purpose of this is to prevent a loss of resolution at extremely low light levels where the analog-to-digital converter might convert meaningful variations to digital zeros. Potentiometers on the back panel of the controller also provide background offset adjustment. The offset value in the software roughly corresponds to the number of counts to offset each pixel, but Roper Scientific states that the actual offset is arbitrary and not of consequence, unless it exceeds 100 counts. The manual accompanying the camera system recommends that the default settings not be changed unless the offset exceeds 100 counts. It also suggests that the offset be measured and subtracted as background.[10]

Background images were acquired in order to compensate for this ADC OFFSET. Without triggering a pulse from the laser, image pairs were acquired where $\Delta t = 0$ (in IEC mode) and $\Delta t = 100$ μs (in ESABI mode). Background image pairs at these temporal separation settings were collected at 10 and 100 kPa. The mean pixel intensity for each image was calculated in the WinView/32 software, and the mean values were themselves averaged. The average pixel reading with no light

entering the camera was measured as approximately 94.3 counts, with a standard deviation of approximately 1.3 counts. This measurement demonstrated no variation with pressure, exposure time, or exposure separation. In order to compensate for this offset, a value of 94.3 counts is subtracted from all pixel intensity values prior to analysis. Since the background measurement also includes signal levels due to thermal charge, background subtraction also has the effect of removing most of the background noise due to thermal charge accumulation.

All image data was stored in the native binary format of the Roper Scientific, Inc.'s WinView/32 software. Each file contains two images where each image is 1300 pixels horizontally by 1030 pixels vertically, and each pixel intensity varies between zero and 4095 counts, rendered on-screen as gray levels.

Once the image files were generated, the WinView/32 software was used to calculate the average pixel intensity over the in-focus portion of each image. Specifically, the mean gray level pixel value on $\{340 < x < 810\} \times \{0 < y < 1030\}$ was calculated for each image. It is emphasized that while the calculations that follow were performed on averaged intensity values, they could also be performed on corresponding pairs of individual pixels.

The ADC OFFSET value of 94.3 counts was subtracted from each mean intensity, giving the values m_1 and m_2 represented by the shaded regions in Figure 5. This figure illustrates the
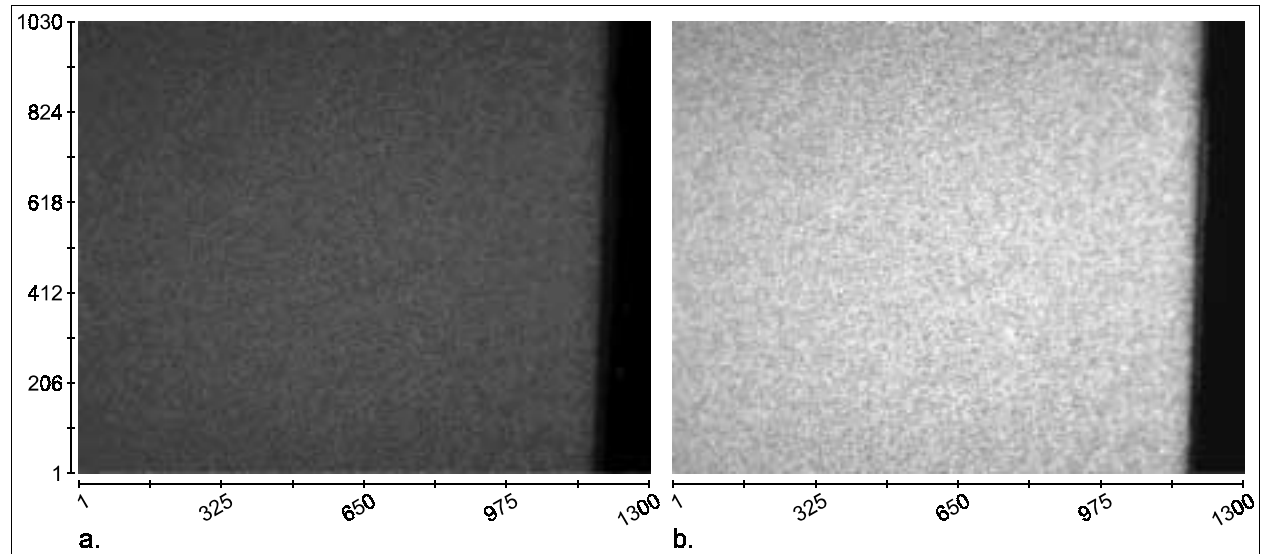

Fig. 6   Two sequential PSP images at 10 kPa acquired by the DIF camera. The first exposure (a.) is 10 μs and the second exposure (b.) is 8.01 ms (10 μs + 8 ms). This pair of images was acquired in IEC mode where the separation Δt between the two images is zero, and therefore the second exposure began immediately upon completion of the first. It is visually apparent that the depth-of-field limits the in-focus region to approximately 340 < x < 810 on the horizontal pixel scale shown.

7

notion that the fluorescence intensity decays in an exponential fashion from some initial brightness I_0 to zero.

Multi-Exponential Fluorescence Decay Model

For the first experiment, a set of image pairs was used to calculate a more precise mathematical model of the fluorescence decay at two static pressures. At pressures of 10 kPa, and repeated at 100 kPa, a sequence of image pairs was acquired where the temporal separation Δt was incremented from 0 to 100 μs in steps of 20 μs. The IEC mode was used to acquire images where the separation time $\Delta t = 0$, and the ESABI mode was used for image separation times $\Delta t > 0$.

The fluorescence decay functions at 10 and 100 kPa will be represented respectively as $f_{10}(t)$ and $f_{100}(t)$, and will be expressed as summed exponentials. Using this as the basis for the model, the measured values m_1 and m_2 at a pressure p represent the integral of the decay function $f_p(t)$ from 0 to 10 μs and from t_2 to t_f (8.01 ms), respectively.

The difference between successive secondary exposures was calculated, as illustrated in Figure 7. This figure demonstrates that the difference between two secondary exposures represents the integrated fluorescence over a partition of the decay curve. For example, consider the secondary images collected where $\Delta t = 40$ μs and $\Delta t = 60$ μs. One image represents the fluorescence decay function integrated from $t_2 = 50$ μs to t_f and the other represents the fluorescence decay function integrated from $t_2 = 70$ μs to t_f. The difference between the two represents the fluorescence decay function integrated from 50 μs to 70 μs.
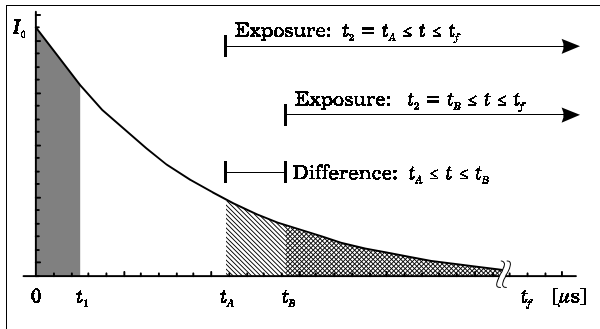

Fig. 7   Difference scheme for partitioning integrated exposure data.

Calculating differences in this manor leads to a list of values representing the integrals of the fluorescence decay function $f_p(t)$ over partitions {(10, 30), (30, 50), (50, 70), (70, 90), (90, 110) μs}.

Additionally, the average of first exposure values at each Δt is used to represent the integral of $f_p(t)$ on the interval (0, 10) μs. Two such lists were calculated, one for data at 10 kPa and the other for data at 100 kPa.

A standard numerical midpoint integral approximation was then applied to each partition.[15] By this approximation, each value can be divided by the partition width and the result is a list of six data points on the curve $f_p(t)$ for each pressure p. The approximated partition areas are illustrated in Figure 8.
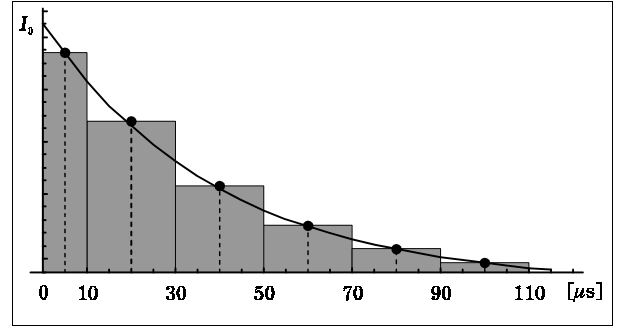

Fig. 8   Midpoint integral approximation of integrated fluorescence decay function partitions.

Since in practice fluorescence decay is best modeled as a sum of several exponential functions,[3] the list of data points shown in Figure 8 was fit to the functional form in equation (4),

$$f_p(t) = \sum_{i=1}^{n} I_i\, e^{-t/\tau_i} \qquad (4)$$

where n is the number of exponential terms to which data points are fit. The parameters I_i and τ_i were obtained by implementing the Levenberg-Marquardt algorithm (a least-squares algorithm that fits data to a nonlinear function) in *Mathematica*. A detailed discussion of the Levenberg-Marquardt algorithm was published by Bevington and Robinson in 1992.[16] The data points were fit to sums of two and three exponentials to compare accuracy. Equation (5) shows the symbolic form with coefficients and time constants calculated by the nonlinear fit to two exponential terms,

$$\begin{cases} f_{10}(t) = 48e^{-t/10.4} + 64e^{-t/41.8} \\ f_{100}(t) = 93e^{-t/11.2} + 21e^{-t/27.7} \end{cases} \qquad (5)$$

8
American Institute of Aeronautics and Astronautics

where the time constants are in μs and the units of the fluorescence intensity coefficients are CCD counts per μs (the units of the coefficients will be discussed presently). Equation (6) shows the results of the nonlinear fit to three exponential terms,

$$\left\{ \begin{array}{l} f_{10}(t) = 61e^{-t/12.8} + 53e^{-t/57.0} - 3.6e^{-t/10^5} \\ f_{100}(t) = 98e^{-t/11.5} + 16e^{-t/32.0} - 0.19e^{-t/10^5} \end{array} \right\} \quad (6)$$

where again, the time constants are in μs and the coefficients have units of counts/μs.

Because m_1 and m_2 represent CCD counts, so too does $\int f_p(t)\,dt$ have units of counts. Therefore, the units of $f_{10}(t)$ and $f_{100}(t)$ are counts per unit time. Counts are proportional to the charge accumulated in a CCD pixel and therefore represent photon intensity integrated over time. Thus, the fluorescence decay expressions $f_p(t)$ in equations (5) and (6) are proportional to the fluorescence intensity as a function of time.

The fit to two exponential terms in equation (5) is more accurate from a physical interpretation. This is because three-exponential functions at 10 and 100 kPa both include terms with a negative coefficient and time constants of 100 ms. The effect of these terms on the analytical functions is that both become negative (at $t = 142$ μs for the 10 kPa curve, and at $t = 153$ μs for the 100 kPa curve) and asymptotically approach zero from the negative side of the horizontal axis. Negative fluorescence intensity has no physical meaning, and thus the functions obtained by fitting the data to the three-exponential form are invalid. The two expressions for fluorescence decay in equation (5) are plotted in Figure 9.

In order to verify these two functions, they are integrated to generate values corresponding to those from the set of second exposures. That is to say, since the second exposure from each pair of images represents the intensity integrated from t_2 to t_f (m_2–see Figure 5), calculating the integrals of the two functions $f_p(t)$ in equation (5) from t_2 to t_f provides a direct comparison of the symbolic form to the values measured at each pressure.

Figure 10 shows measured values m_2 plotted by symbols at corresponding values of t_2. It also shows as curves the fluorescence intensity functions integrated from t_2 to t_f plotted as t_2 was varied. This plot verifies the accuracy of the two fluorescence decay models.
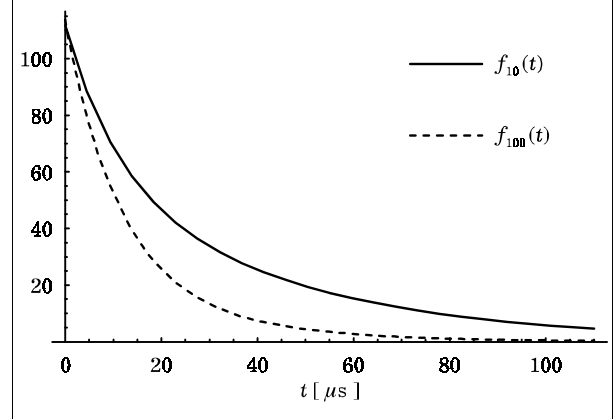

Fig. 9 **Modeled exponential fluorescence decay functions** $f_{10}(t)$ **(fluorescence decay at 10 kPa) and** $f_{100}(t)$ **(fluorescence decay at 100 kPa).**
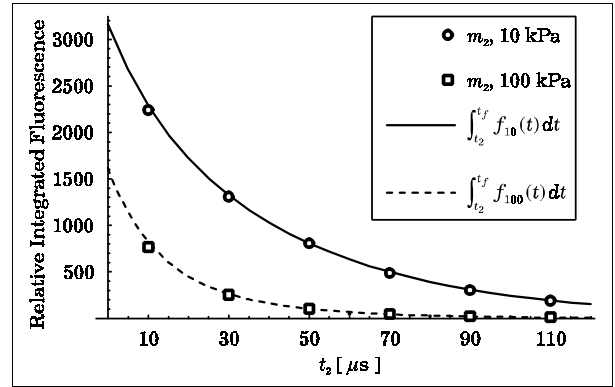

Fig. 10 **Fluorescence decay integrated from** t_2 **to** t_f **(8.01 ms), plotted as a function of** t_2. **The discrete points labeled** m_2 **(at 10 kPa and 100 kPa) represent second-exposure values plotted at corresponding ESABI** t_2 **values, as defined in figure 5. The solid and dashed curves are calculated from the** $f_p(t)$ **functions to illustrate the accuracy of the fluorescence decay model.**

Direct Pressure Measurement

For this experiment, the pressure was varied from 10 kPa to 100 kPa in steps of 20 kPa. Image pairs were acquired at each pressure using the ESABI mode of the DIF camera with $\Delta t = 20$, 50, and 80 μs. The fluorescence decay was approximated by a single exponential function, so that a decay time constant τ could be calculated from each pair of images. The error introduced by this approximation will be addressed.

By assuming a single exponential fluorescence decay, the integral expressions for m_1 and m_2 in Figure 5 can be calculated as shown in equations (7) and (8),

$$m_1 = \int_0^{t_1} I_0\, e^{-t/\tau}\, dt = I_0 \tau \left(1 - e^{-t_1/\tau} \right) \quad (7)$$

9

$$m_2 = \int_{t_2}^{t_f} I_0\, e^{-t/\tau}\, dt = I_0\tau\, e^{-t_2/\tau} \qquad (8)$$

where I_0 is the fluorescence intensity at $t = 0$, and $t_f \gg \tau$ so that $\mathrm{Exp}[-t_f/\tau] \approx 1$. Since $t = 0$ marks the start of the first exposure, $t_1 = 10\ \mu$s. The ratio of equations (7) and (8) is shown in equation (9),

$$\frac{m_1}{m_2} = e^{t_2/\tau} - e^{\Delta t/\tau} \qquad (9)$$

where t_2, Δt, and τ have units of μs and $\Delta t = t_2 - 10$ μs. Thus, given the measured values m_1 and m_2 where the second exposure commenced at a time Δt after the first exposure ceased, τ can be obtained by numerically solving equation (9). Values for the time constant τ were calculated from image pairs acquired at each pressure and exposure separation time. The results are plotted in Figure 11; note that the horizontal pressure axis is logarithmic.

A significant feature of the graph in Figure 11 is the fact that relationship between the pressure and the fluorescence decay time constant shifts vertically according to the exposure separation time Δt. This is the effect of error introduced by the one-exponential approximation. The cause of the error is best explained by comparing the more accurate decay function in equation (5) to the results plotted in Figure 11. For example, consider the 10-kPa fluorescence decay function in equation (5): $f_{10}(t) = 48\, e^{-t/10.4} + 64\, e^{-t/41.8}$. There are two terms signified by two time constants. Considered separately, the first term with the shorter time constant decays to one percent of its initial value at $t = 47.9\ \mu$s. The second term with a greater time constant decays to one percent of its initial value at $t = 193\ \mu$s. The effect of this on m_2 (i.e., on an integral from t_2 to t_f) is that for greater values of t_2, the contribution by the short-lived component is small. Thus, the integrated fluorescence decay is dominated by the second, longer-lived exponential component for large values of t_2. For smaller values of t_2, the integral includes a more significant contribution from the short-lived exponential term.
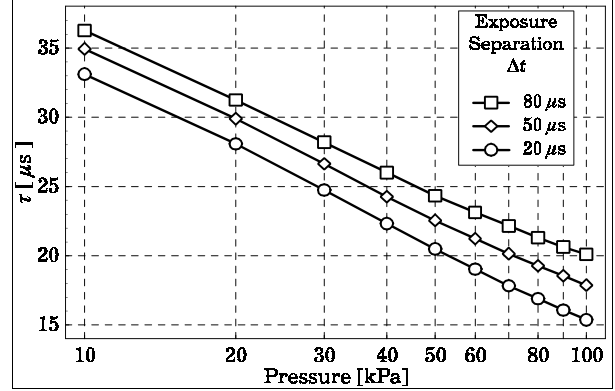

Fig. 11   Single-exponential time constants expressed as a function of pressure at three ESABI separation times. Note that the horizontal pressure scale is logarithmic.

This can be related to the single exponential approximation of the fluorescence decay. The time constant obtained by this approximation will be a weighted average of the two time constants observed in the two-exponential decay function. The weighting comes from the significance of each component over the two integrated regions m_1 and m_2. In other words, as Δt is increased, the contribution to m_2 by the short-lived exponential term decreases, and the approximation more closely resembles the long-lived term. As Δt is made smaller, the contribution from the short-lived exponential term becomes more significant, and the approximation yields a smaller value of τ. This is evident in Figure 11, where the value of τ increases (shifts the line vertically upward) with increased Δt.

The vertical displacement of curves in Figure 11 demonstrates error in a single-exponential model of fluorescence decay. However, while the approximation is not accurate for the purposes of modeling the fluorescence decay, the time constant given by the approximation at a particular ESABI interval Δt is consistent with respect to pressure. Figure 11 shows that the relationship between the decay time constant and natural logarithm of the pressure is approximately linear for a given Δt. As a result, the time constant obtained from a single-exponential approximation of the fluorescence decay can be used to calculate pressure.

Each of the three data sets plotted in Figure 11 was fit to the symbolic form $\tau(p) = a - b \ln p$. Values for the parameters a and b at each Δt were obtained by implementing the Levenberg-Marquardt algorithm with all three sets of data points. The resulting expressions were then algebraically

manipulated to obtain the $p(\tau)$ relationships shown in equation (10),

$$p(\tau) = \begin{cases} 694\, e^{-\tau/7.84} \text{ kPa}; & \Delta t = 20\,\mu s \\ 1040\, e^{-\tau/7.51} \text{ kPa}; & \Delta t = 50\,\mu s \\ 1610\, e^{-\tau/7.11} \text{ kPa}; & \Delta t = 80\,\mu s \end{cases} \quad \textbf{(10)}$$

where τ is in μs.

To conclude, this application of the DIF camera to PSP measurements begins by acquiring double-image data such as that in Figure 11, specific to the PSP to be used in an experiment. The points at a particular ESABI separation Δt are fit to a single exponential. This gives a relationship between the time constant τ and the pressure p. Once this relationship is established, DIF image pairs of a dynamic pressure system can be acquired. Absolute pressure can then be calculated on a per-pixel basis from each image pair directly, with no need for wind-off measurements.

Phase Measurements With An ITCCD

In addition to dual image operation, recent laboratory studies at CSM have shown that the ITCCD can also be used in resolving phase. Homodyne and heterodyne processes are very similar frequency translation processes. The difference between the two schemes lies in the frequency of the local oscillator used for frequency translation. Homodyne detection utilizes a local oscillator that has its frequency and phase terms matched to a modulated input signal. Thus, the input signal is convolved down to a dc component, and only the magnitude information is retained.[17]

The heterodyne receiver mixes a modulated input signal with a sinusoidal function that has a frequency term that is different than the modulation, carrier frequency. By sampling the input, modulated at a carrier frequency f_c with a sinusoid at a sampling frequency f_s that differs from f_c, the input information is convolved down to an intermediate frequency (IF). The IF is the difference between the modulation frequency f_m and the sampling frequency f_s. Since the input has been translated to a different, lower frequency (above dc), both magnitude and phase information are preserved.[18]

The ITCCD architecture can also be used in a continuous time, heterodyne mode. Essentially, the ITCCD can be operated as a natural sampler at a particular sampling frequency f_s. Rather than capture a single exposure in the vertical register, as illustrated in Figure 2, multiple exposures can be integrated into one image, which is held in the vertical register. Integrating multiple exposures at the sampling rate f_s into the vertical register is accomplished by pulsing both the ROG barrier and the OFD barrier at the sampling frequency f_s and an exposure time τ_s. The two barriers are operated a half cycle out of phase from each other so that when one barrier is high the other is low.

The sampling process can be modeled as the natural sampling function $q(t)$,

$$q(t) = \psi_s \sum_{n=-\infty}^{\infty} \text{Sa}(\pi\, n\, \psi_s)\, e^{j 2\pi f_s n t} \quad \textbf{(11)}$$

where ψ_s is the duty cycle and $j = \sqrt{-1}$. If two inputs $m(t)$ and $f(t)$ are present and they are at the same frequency but have different phase components, then the phase differences can be resolved at the output of the imaging system. Since the inputs are optical, a dc term A_o is added to the definitions.

$$m(t) = A_o + A_m \cos(2\pi f_m t + \theta_m) \quad \textbf{(12)}$$

$$f(t) = \varepsilon A_o + \varepsilon A_m \cos\left[2\pi f_m t + (\theta_m + \phi_f)\right] \quad \textbf{(13)}$$

The natural sampling function $q(t)$ is comprised of a dc component, the fundamental sampling frequency component, and all the odd harmonic components. The higher order harmonics however will be filtered out by the frame rate of the imaging system, which acts as a lowpass filter. Using a framing period T_f, the filtering process produced by the system's frame rate can be modeled as a sample and hold function, which has the power transfer function $|H_{sh}|^2$.

$$\left|H_{sh}(f)\right|^2 = \left|Sa\left(\pi f T_f\right)\right|^2 \quad \textbf{(14)}$$

Thus, after mixing the modulated input with the natural sampling function, the higher order frequency components will be filtered out and only the dc component and the IF component f_I remain. The magnitude and phase information is contained at the IF.

$$m(t)\,q(t) = C\cos(2\pi\,f_I\,t + \theta_m) \qquad \textbf{(15)}$$

$$f(t)\,q(t) = C_\varepsilon \cos\!\left[2\pi\,f_I\,t + (\theta_m + \phi_f)\right] \qquad \textbf{(16)}$$

If for example, the input $m(t)$ is a modulated cw laser used as an excitation source, and the input $f(t)$ is the resulting fluorescence from a PSP experiment, then the phase difference between the two signals can be determined. The phase difference can then be utilized with lifetime technique calculations to determine pressures and temperatures. An experiment where this is implemented is presently being planned.

Concluding Remarks

Significant advances in CCD camera technology have been made in recent years. A commercially available product provides the ability to acquire high-speed sequential images with extremely precise timing. Initial experiments have also demonstrated that an ITCCD can also be used as a heterodyne detector to resolve a signal phase.

A PSP experiment featuring the double-image system was conducted. Analysis of data taken over a range of static pressures demonstrated the ability to calculate pressure directly from image pairs without the need for "wind-off" reference images. Double-image data as the temporal separation between images was varied was also acquired. Analysis of this data demonstrated the ability to produce more elaborate models of PSP fluorescence decay.

Further double image and heterodyne experiments are planned.

Acknowledgments

References

[1] L. P. Goss. "Pressure-sensitive paint specification sheet–Pt(TfPP)-FIB-Based PSP." *Innovative Scientific Solutions, Inc.* March, 1999.

[2] J. R. Lakowicz (editor). *Topics in Fluorescence Spectroscopy–Volume 2, Principles* New York, NY: Plenum Press, 1991, §2.2.1.

[3] A. Sharma and S. G. Schulman. *Introduction to Fluorescence Spectroscopy.* New York, NY: John Wiley & Sons, Inc., 1999, ch 1, 2, and 4.

[4] Oglesby, D. M., Chith, K. P., and Upchurch, B. T. "Optimization of measurements with pressure sensitive paints." *NASA Technical Memorandum 4695*. NAS 1.15:4695, June 1995.

[5] Sajben, M. "Uncertainty estimates for pressure sensitive paint measurements." *AIAA Journal*, Vol. 31, No. 11, pp. 2105-2110, Nov. 1993.

[6] W. L. Weaver, J. D. Jordan, G. A. Dale, and K. R. Navarra. "Data analysis methods for the development and deployment of pressure-sensitive paints." *37th AIAA Aerospace Sciences Meeting and Exhibit*, Reno, NV, AIAA 99-0565, 1999.

[7] R. C. Crites. "Pressure sensitive paint technique." *VKI, Measurement Technology*, Rhode Saint Genese, Belgium : von Karman Institute for Fluid Dynamics, 1993.

[8] J. F. Donovan, M. J. Morris, A. Pal, M. E. Beene, and R. C. Crites. "Data analysis techniques for pressure- and temperature-sensitive paint." *31st AIAA Aerospace Sciences Meeting & Exhibit*, Reno, NV, AIAA 93-0176, 1993.

[9] Y. Shimbo, K. Asai, H. Kanda, Y. Iijima, N. Komatsu, S. Kita, and M. Ishiguro. "Evaluation of several calibration techniques for pressure sensitive paint in transonic testing." *20th AIAA Advanced Measurement and Ground Testing Technology Conference*, Albuquerque, NM, AIAA-98-2502, 1998.

[10] Roper Scientific (Princeton Instruments, Inc.). *MicroMAX System Manual*. Trenton, NJ, 1998.

[11] E. L. Dereniak and D. G. Crowe. *Optical Radiation Detectors*. New York, NY: John Wiley & Sons, Inc., 1984.

[12] J. R. Janesick, T. Elliott, S. Collins, M. M. Blouke, and J. Freeman. "Scientific charge-coupled devices." *Optical Engineering*, Vol. 26, No. 8, 1987, pp. 692-714.

[13] C. W. Fisher, M. A. Linne, N. T. Middleton, G. J. Fiechtner, and J. R. Gord. "Phase sensitive imaging in flows." *37th AIAA Aerospace Sciences Meeting and Exhibit,* Reno, NV, AIAA 99-0771, 1999.

[14] Sony. *Semiconductor Selection Guide–CCD Camera System*. May 1999.

[15] W. Cheney and D. Kincaid. *Numerical Mathematics and Computing, 4th ed.* Pacific Grove, CA: Brooks/Cole Publishing Company, 1999, §5.1.

[16] P. R. Bevington and D. K. Robinson. *Data Reduction and Error Analysis for the Physical Sciences, 2nd ed.* Boston, MA: WCB/McGraw-Hill, 1992, §8.6.

[17] F. G. Stremler. *Introduction to Communication Systems, 3rd ed.* Reading, MA: Addison-Wesley Publishing Co., Inc., 1990.

[18] T.E. French. "The Development of Fluorescence Lifetime Imaging and An Application in Immunology." Ph.D. Thesis, University of Illinois at Urbana-Champaign, 1996.